Powder Technology 330 (2018) 371–385

Contents lists available at ScienceDirect

Powder Technology

journal homepage: www.elsevier.com/locate/powtec

Detection and estimation of capillary interparticle forces in the material of a fluidized bed reactor at high temperature by powder flow characterization

Roberto Chirone [a,*], Diego Barletta [b], Massimo Poletto [b], Paola Lettieri [a]

[a] Department of Chemical Engineering, University College London, London WC1E 7JE, UK
[b] Dipartimento di Ingegneria Industriale, Università degli Studi di Salerno, Via Giovanni Paolo II, 132-I-84084 Fisciano, SA, Italy

ARTICLE INFO

Article history:
Received 24 September 2017
Received in revised form 10 January 2018
Accepted 9 February 2018
Available online 15 February 2018

Keywords:
Fluidised bed reactor
High temperature
Interparticle forces
Capillary forces
Powder flow properties
Fine particles
Cohesiveness

ABSTRACT

Two ceramic powder samples having different compositions of surface impurities and particle size distributions were considered. These two samples resulted from a high temperature fluidized bed reactor which in its operation showed changes of working condition that might be attributed to the onset of strong interparticle forces. The flow behaviour of these powders was characterized by the High Temperature Annular Shear Cell (HT-ASC), between ambient temperature and 500 °C. Furthermore, a model is developed to relate the change of the powder flowability to the formation of a liquid phase due to the melting of particle impurities present on the particle surface. In particular, the model is used to predict, on the base of the salt composition, the intensity of the interparticle forces at different temperatures. The interparticle forces predicted by the model can be compared with those that can be inferred from the powder flow properties measured with the HT-ASC. Therefore, it is demonstrated that it is possible to derive a theoretical model to predict interparticle forces in a particulate material relevant to fluidized bed reactor, on the basis of the impurities composition. Furthermore, it is demonstrated the possibility to correctly estimate the intensity of average interparticle forces in the same kind of material by the interpretations of bulk flow properties measured with a shear tester, even in the case in which capillary forces take the place of the much weaker van der Walls forces. More in general, the paper suggests a method by which powder rheology can be used to indirectly evaluate the effects of the interparticle forces on fluidization processes even in case in which strong capillary interaction occur.

1. Introduction

It is well recognized the role that fluidized bed reactors and other unit operations have played for a wide range of industries, including energy, nuclear, chemicals, pharmaceutical and other process industries [1]. In particular, recently fluidized bed reactors encountered a great interest with regard to the production of clean energy (combustion and gasification from renewable sources) and waste incineration of solids material [2,3]. Although fluidized bed systems offer several advantages such as high heat transfer rate, rapid solids mixing, large surface contact, high heat and mass transfer rates between gas and particles, a complete understanding of the phenomena occurring in these reactors is still a challenge, with reference to the role of the process conditions [4,5], such as pressure, temperature and humidity. Often, the operating conditions of these processes, with reference to temperature and pressure, are different from ambient values [6]. Hence, the understanding of temperature effects on the system behaviour is crucial for the correct operation of several industrial process units, including fluidized bed units performing reactions, granulation and drying [1].

The powder flowability is affected by many different particle properties, such as particle size shape, size distribution as well as roughness of particle surface [7,8] and other particle mechanical properties [9–13]. In particular, Fu et al. [8] measured the flow properties of three different samples of lactose, two of them with the same size distribution and different particle shape and the other sample with particle having the same shape factor but different size distribution. The results show that differences in particle size distribution and, particularly, particle shape, significantly affect flow properties of the powders. Differently, Pilpel and Britten [10] carried out measurements on the flow rates and on the tensile strength of different powders from ambient to 200 °C. They explained the results in terms of the temperature dependency of material hardness and elasticity. Also Tomas [11,12] looked at the hardness of the particles to describe the flow properties of different powder samples. He developed a model to relate microscopic interparticle forces to bulk flow properties, which account for elastic-plastic particle deformation at the contact points. More recently, Medhe et al. [13] successful applied this model to analyse the flow properties of fine cohesive

* Corresponding author.
E-mail address: roberto.chirone.13@ucl.ac.uk (R. Chirone).

https://doi.org/10.1016/j.powtec.2018.02.024
0032-5910/

powders evaluated with the Jenike shear tester. Direct experimental measure of interparticle forces with AFM are reported in the literature for adhesion [14] and for friction [15]. An attempt to relate AFM measurements of interparticle forces for dry fine powders was given by Castellanos and co-workers [16,17].

Moreover, many authors have also studied the effect of operating conditions such as the system temperature [18–21], the particle size distribution [22] and shape [23], the system humidity [7,24–27] on the flow properties.

Kanaoka et al. [18] have focused on the effect of temperature, up to 900 °C, on the adhesive properties of fly ash particles resulting from coal combustion. They observed a slight change of adhesive forces and internal friction angle up to 700 °C, while a significant increase of these variables was found for temperatures higher than 850 °C. Furthermore Tomasetta et al. [19] and, later, Chirone et al. [28] used the high-temperature annular shear cell developed at the University of Salerno to measure the bulk flow properties of several powder samples characterized by different particle materials and particle size distributions. The equipment used was able to explore temperature effects between ambient temperature and 500 °C. In spite of the indication that in the studied particulate systems only van der Waals interparticle forces could be relevant, a significant increase of powder cohesion at 500 °C was observed by Chirone et al. and, coherently, a lower flowability of the samples. Experiments carried on Titanium oxide Powders allowed to define the role of the material hardness on the estimation of van der Waals interparticle forces [20]. Experiments on widely distributed ashes and coal allowed to understand and account for the effect of wide particle size distributions [21,22]. Multiple interparticle contacts were considered in order to account for irregular shapes [23].

Pierrat and Caram [24] developed a model in order to predict the tensile strength of wet granular materials and also proposed a theory to reduce the number of tests to be performed in the investigation of the effect of moisture on the flow properties of granular materials [25]. They also proposed a correlation that fitted well with experimental measurements carried out on glass beads of 93 μm diameter and suggested the theory of shift. According to this theory it is possible to determine the yield locus of a powder at any moisture content by shifting the original failure function in the region of positive normal stresses. Lately, Landi et al. [26] used the bridge model by Pierrat and Caram [24] considering the roughness of the particles. Their model was based on the hypotheses of capillary condensation and allowed the correct determination of the capillary forces. Besides, the model prediction of the powder tensile strength agreed well with the estimates of the tensile strength, derived from direct powder shear tests carried out at air relative humidity up to 80%. A similar model was very recently applied by La Marche et al. [29] to estimate capillary forces in beds of glass beads fluidized with humid air. In that case, the model was perfected by introducing two scales in the asperity size. The result was that the predicted capillary interparticle forces could show a change in the intensity of the force with relative humidity, larger than found by Landi et al. [26]. La Marche et al. [29] used AFM to characterize the particle surfaces and measure the two asperity sizes. Furthermore, Cohesive Discrete Element Method (CDEM) has been performed to investigate the internal tensile stress and the tensile strength of fine, cohesive wet granular materials [27]. Althaus et al. [30] studied the rheology of fine wet powders in pendular state. They found that the angle of internal friction is not much dependent on consolidation and liquid viscosity and that the yield locus of the wet mixtures could be determined by the isostatic tensile strength of the material predicted by the Rumpf [31] approach from theoretical estimates of the capillary forces.

In fluid bed reactors, interparticle forces set up without consolidation or with very low consolidation [32,33]. Kono et al. [32] developed a new useful method to define the rheological properties of aerated fine powder. They found a qualitative correspondence between some rheological parameters and freely bubbling characteristics in two-dimensional fluidized beds. Bruni et al. [33] studied the influence of interparticle forces on the fluidization behaviour of fine Geldart [34] group A powders as a function of the size distribution of the fine subcuts (particles below 45 μm) and of the temperature. Valverde and Castellanos [35] based their research on the fluidization of nanoparticles. They proposed a simple equation to estimate the size of the agglomerate formed in a fluidized bed reactor solving the balance between the local shear force on the particle attached the agglomerate and the interparticle adhesion force. Shabanian and Chaouki [36] focused their studies on the effect of interparticle forces at high temperature, 700–1000 °C, on the bubbling fluidization behaviour of coarse particles. Experimental findings revealed that the flow dynamics of a bubbling bed of coarse particles at high temperature was mainly influenced by the variation of the gas density with temperature when interparticle forces did not play a significant role. However, when the interparticle forces are relevant in the system, a multiplicity of behaviors can occur at elevated thermal levels. Mikami et al. [37] studied the fluidization of bed of metal particles exposed to temperatures producing particle sintering by surface diffusion. They found a good correlation between interparticle forces estimated applying the Rumpf [31] approach on the measured compressive strength of agglomerates and the fluidization overpressure necessary to break the sintered bed. Later, Seville et al. [38] approached the agglomeration process of metal particles at high temperature by comparing the sintering characteristic times assuming a viscoplastic behaviour of the particles and the characteristic times for quiescent motion of particles in the fluidized bed. In that case it was deduced that the compressive interparticle forces estimated with the Rumpf [31] approach does play a significant role in particle agglomeration by sintering at high temperatures.

The gravity flow of aerated powder is controlled by the relative magnitude between the interparticle cohesive forces, the resultant of the particle weight and the fluid dynamic interactions [39–42]. In addition, it must be considered that in the case of high temperature processes, the intensity of interparticle cohesive forces, such as capillary, electrostatic and van der Waals forces, can be different from ambient values. These changes are principally due to the variations of particles hardness, liquid bridge formation and modification of the particle dielectric properties.

In case of only van der Waals forces, Mutsers and Rietema [39] and Rietema and Piepers [41] found that the cohesiveness of the particles acts as controlling factor of the formation of the expanded bed. Moreover, Massimilla and Donsì [43] stated that the sites at which contact takes places are the asperities and therefore the adhesion force depends on the surface topology. Also the emergence of capillary forces in presence of capillary bridges can significantly affect the fluidization behaviour of powders [44]. In fact, they can be much more significant than other interparticles forces even in processes at ambient temperature [45]. Concavity in capillary bridges allows water condensation at air humidity below saturation [29,46–48]. Liquid bridges between particles can also be determined by the system moisture [49]. In fluidized beds capillary forces modify bed properties such as voidage, channels and aggregate size, which in turn determine the average bed permeability [50]. All these effects can be indirectly attributed to the increase of powder cohesion due to capillary forces [24,25,51,52]. D'Amore et al. [50] analyse the influence of moisture on the behaviour of a fluidized bed of non-porous and porous materials. They found that the particle porosity is one of the key parameters in determining the relationship between moisture and bed properties. Also Seville and Clift [53] and, later, Wormsbecker and Pugsley [54] reported on the effects of liquid bridges on the fluidization characteristics of fine particles. They observed in the fluidized bed behaviour a transition from that of group A to that of group C of the Geldart classification with the increasing amount of liquid in the system. It is believed, therefore, that in high temperature processes the presence of surface impurities, with relatively low-melting temperature, can determine the formation of capillary liquid bridges giving rise to unexpected flow behaviour [55].

In this paper, two ceramic powder samples having different compositions of surface impurities and particle size distributions were

considered. These two samples resulted from a high temperature fluidized bed reactor, which showed changes of the working conditions in the operation that might be attributed to the onset of strong interparticle forces. In spite of the apparent similarity with the systems studied by Chirone et al. [28] the materials considered in this paper are "real" industrial powders. In these 'real' systems the estimation of capillary interparticle forces requires an evaluation of the amount of the liquid available for the formation of capillary bridges at the operating temperatures, as well as the correct estimation of the contact geometry. Therefore, the main objective of this paper is the definition of a procedure in which the results of the experimental characterization of the surface particle impurities including qualitative and quantitative information leads to the estimation of the interparticle forces as a function of temperature. In order to verify the results of this procedure, the obtained interparticle forces are compared, in this paper, with the forces estimated from the powder flow properties measured by the High Temperature Annular Shear Cell (HT-ASC), between ambient temperature and 500 °C. In particular, the force estimation procedure from HT-ASC results follows closely the procedure previously proposed by Chirone et al. [28]. However, as it will appear clearly in the following, the effect of temperature on the powders studied in this work is significantly stronger and significantly not linear with temperature, coherently with the hypothesis of the onset of capillary interparticle forces. This circumstance has inspired the definition of a new experimental procedure with HT-ASC to rapidly identify the temperature of the onset of capillary forces.

2. Theoretical background

Interparticle forces can be the result of three different mechanisms of adhesion as reported by Israelachvili [56], van der Waals interactions, capillary bridges and electrostatic forces. The first two of these are those of interest in this paper. Following Rumpf [31] and Molerus [9] approach, it is possible to correlate the powder tensile strength of the powder, σ_t, with the particle-particle interactions. Accordingly, σ_t can be related to the mean attractive interparticle force, F_{int} by the following relationship:

$$\sigma_t = \frac{kF_{int}}{d_{sv}^2}\frac{1-\varepsilon}{\pi} = \frac{F_{int}}{d_{sv}^2}\frac{1-\varepsilon}{\varepsilon} \tag{1}$$

where d_{sv} is the Sauter mean diameter, ε the powder void fraction and k is the number of contact points on each particle that is estimated by means of the relation $k\varepsilon = \pi$ as proposed by Rumpf [31] according to Smith et al. [57]. Eq. (1) is very simple and, to be obtained, it requires a number of simplifying assumptions. In the appendix, these assumptions are listed and discussed in order to understand the potential limits of validity of Eq. (1).

With the hypothesis of a perfectly plastic deformation at the contact points between particles, Molerus [9] developed his model for the adhesion due to van der Waals forces as a function of the consolidation force at the contact point F_N:

$$F_{vdW} = \frac{A^* r_{pla}}{12 z_0^2}\frac{1+\left(2F_N/\pi p_f r_{pla} z_0\right)}{1-\left(A^*/6\pi p_f z_0^3\right)} \tag{2}$$

where A^*, r_{pla}, p_f and z_0 are the Hamaker constant, the mean curvature radius at contact points, the material compressive strength at particle contact and the separation distance between the molecular layers of the two contacting surfaces [58] respectively. It should be remarked that r accounts for the irregularities of the particle shape and asperities and, therefore, it is not necessarily related to the particle size. In absence of other information, Molerus [9] suggests to adopt for p_f a value that is three times the unconfined yield strength of the material. In cases in which van der Waals forces are supposed to be the sole interparticle forces, then it can be assumed that $F_{int} = F_{vdW}$. This model has been used to correlate the strength of the powder to the particle-particle interactions. For further information see Chirone et al. [28].

In case of presence of a liquid phase, surface tension may determine the formation of connecting links between the particles, named capillary bridges, that result in attractive forces between particles (see for example Fayed and Otten [59]). These forces depend on the local particle curvature. Therefore, with perfect spheres, they depend on the particle size. Instead, with rough particle surfaces, liquid bridges form between particle asperities and the asperity size should be properly considered for the estimation of the effective curvature radius at contacts. Following the approach proposed by Landi et al. [26], it is possible to describe the characteristics of the formed capillary bridge according to the simplified approach used by Rabinovich et al. [60].

$$r_1 = r_{pla}\left[\left(1+\frac{a}{2r_{pla}}\right)\sec\beta - 1\right] \tag{3}$$

$$r_2 = r_{pla}\left[\left(1+\frac{a}{2r_{pla}}\right)\tan\beta - \left(1+\frac{a}{2r_{pla}}\right)\sec\beta + 1\right] \tag{4}$$

$$\begin{aligned} V_b = {} & 2\pi\left[r_1^2 + (r_1+r_2)^2\right] r_1\cos\beta - \left(\frac{2\pi\left(r_1^3\cos^3\beta\right)}{3}\right) \\ & -2\pi r_1^2(r_1+r_2)\left[\cos\beta\sin\beta\left(\frac{\pi}{2}-\beta\right)\right] + \\ & -\frac{2\pi r_{pla}^3(2+\cos\beta)(1-\cos\beta)^2}{3} \end{aligned} \tag{5}$$

where r_{pla} is the curvature radius at the contact point assumed to coincide with curvature radius of the asperity, a is the gap between the bridge asperity and β is the angle of the wet spherical cap of the contact measured from the centre of the curvature radius as defined in Fig. 1. Rearranging Eqs. (3) to (5) the volume of the bridge is a function of a single parameter, which is the angle β. Inversely, if the volume of the bridge is set, as well as the radius of the contact point, then it is possible evaluate the bridge geometrical characteristics, i.e., r_1, r_2, and β. In turn, according with the theoretical model of capillary bridges proposed by Pierrat and Caram [24], these parameters allow to derive the tensile force of the bridge, F_c^*. In particular, this force can be considered as the sum of the direct action of the surface tension σ_s in the axial direction of the bridge and in its indirect effects through the pressure difference generated by its action on the capillary bridge surface.

$$F_c^* = 2\pi r_2\sigma_s + \pi r_2^2\sigma_s\left(\frac{1}{r_1}-\frac{1}{r_2}\right) \tag{6}$$

If capillary forces are present, generally these are much larger than van der Waals forces [60] and, therefore, it is possible to neglect these latter and assume that $F_{int} = F_c^*$.

3. Experimental

3.1. Apparatus

The apparatus used to measure the powder yield loci between ambient temperature and 500 °C is the High Temperature-Annular Shear Cell (Fig. 2) described by Tomasetta et al. [61]. The main geometric properties are listed in Table 1. The working temperature is ensured by two electric heaters placed in the lid and in the bottom ring which provide a maximum operating temperature of 500 °C. In particular, three thermocouples (type "J") are placed at different depths of the powder sample and the temperature uniformity inside the cell is controlled by a PID temperature control system.

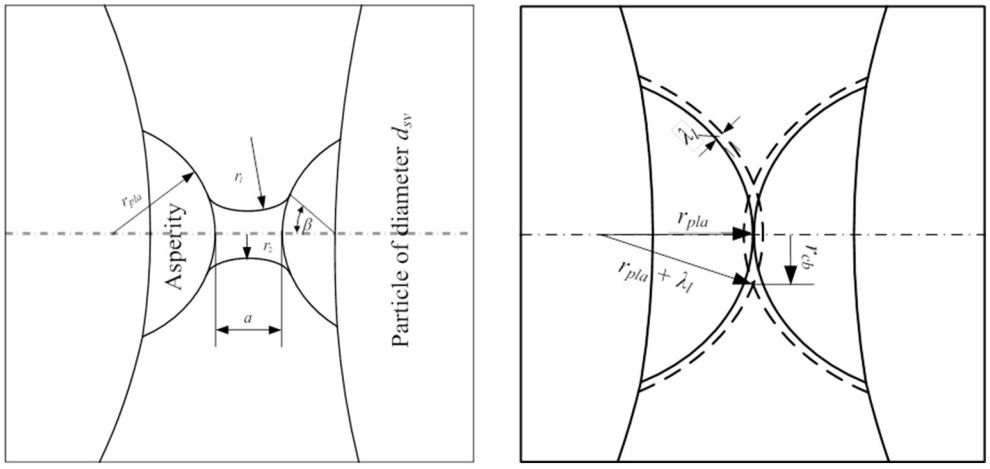

Fig. 1. Schemes of the contact with nomenclature definition. a) capillary bridge; b) particle asperity with impurities.

3.2. Materials

Experiments were carried out on two powders samples provided by an industrial partner. The samples have the same kind of mother particles with different particle size ranges and different amounts of impurities. These impurities have been accumulated during a reactive treatment process. The first sample ("A") and the second sample ("B") contain an intermediate and a high level of impurities respectively. Unfortunately, other details of the material cannot be provided for confidentiality reasons.

A laser scattering particle size analyzer Mastersizer 2000 (Malvern Instruments) was used to measure the particle size distributions of the samples and to scan the sample surfaces. Results are reported in Fig. 3 and in Table 2 in terms of the Sauter mean diameter, d_{32}, that is the surface weighted mean size, the volume weighted mean size, d_{43}, and the sizes corresponding to the 10th, the 50th and the 90th percentile of the volumetric distribution, named d_{10}, d_{50}, and d_{90}, respectively. Both materials belong to the Group A of the Geldart classification for fluidization behaviour.

The sample surfaces were observed with a Scanning Electron Microscope (SEM). Fig. 4 reports typical SEM images obtained on the different samples. Inspection of Fig. 4 shows comparable aspects for the two samples such as large amounts of fines adhering on the surface of larger particles, irregularly shaped particles with flat surfaces and relatively sharp edges. Moreover, the specimen B, richer in impurities, exhibits a great number of sticking particles, which seem to be partially sintered on the larger particles.

Also, Energy Dispersive X-ray spectroscopy (EDX) analyses have been performed on the two samples. Results are reported Fig. 5. These results show the presence of several impurities. In particular, the most abundant are aluminum, calcium and chlorine. Based on the process characteristics, it is assumed that the three are present in form of aluminum chloride ($AlCl_3$) and calcium chloride ($CaCl_2$). Moreover, impurities in Fig. 4 appear as a separate solid phase on the particle surface. As a result, the melting temperature of the impurities should not be affected by their amount in respect to the mother ceramic powders. Details on the composition of the impurities are provided and discussed in the Model Results Section 4.2, below.

A SDTQ600 (TA Instruments) was used to carry out both Differential Thermal Analysis (DTA) and Thermal Gravimetric Analysis (TGA). The purpose was to put in evidence any possible phase transitions or chemical reactions in the range of the temperatures tested with the HT-ASC.

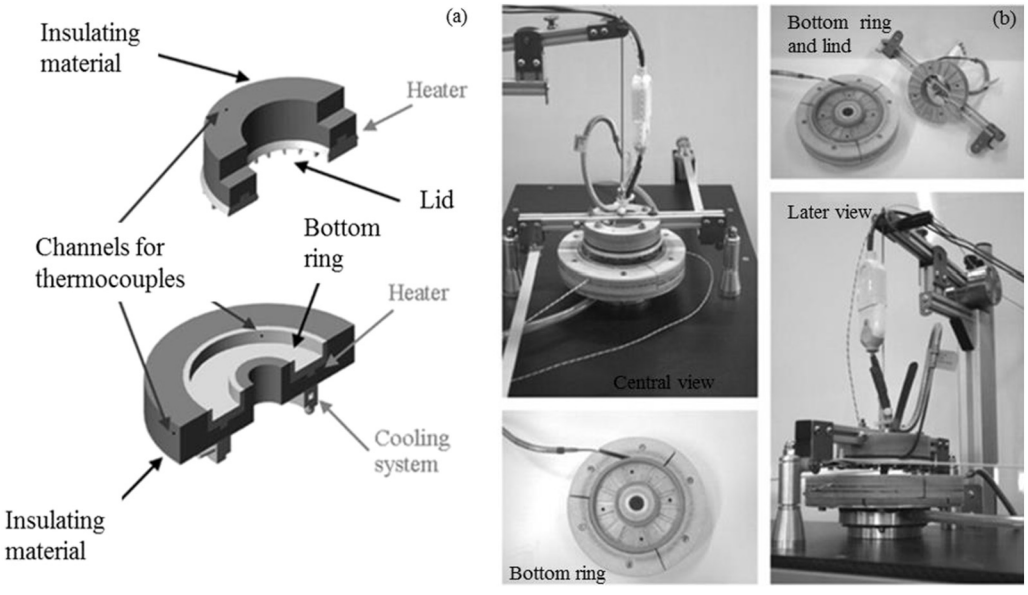

Fig. 2. Schematic representation (a) and pictures (b) of the high temperature annular shear cell.

Table 1
Geometric properties of the HT-ASC.

Bottom ring	Inner diameter, mm	60
	Outer diameter, mm	120
	Nominal height, mm	10
	Internal volume, m^3	95
Lid	Inner diameter, mm	62
	Outer diameter, mm	118
Electric heaters	Bottom heater, W	600
	Lid heater, W	260

Table 2
Characteristic particle sizes of the samples tested.

Sieving range, μm	Sample "A"	Sample "B"
d_{10}, μm	6	13
d_{50}, μm	25	44
d_{90}, μm	85	180
d_{32}, μm	14	21
d_{43}, μm	37	76

DTA and TGA were performed in air and nitrogen and the temperature program adopted ensure a linear rate temperature increase, 10 °C/min, from 25 °C to 550 °C. Unfortunately, it was not possible to have heat calibrated signal for the DTA, whose response in terms of heat exchanged has to be taken only qualitatively. In Fig. 6a–b the heat flow and the sample weight change, related to the weight at ambient temperature, are reported as a function of temperature for both "A" and "B" samples. All measured heat fluxes are positive, that is they are intended towards the sample. Phase changes should be visible with fluxes larger in modulus as negative peaks. Accordingly, inspection of the figure reveals a similar thermal behaviour of the two powders. In particular, it can be observed that it is not possible to detect any significant phase change, either melting or solid phase transition, above 300 °C where the materials tested show the largest effect of temperature in the industrial process. A change of weight is detected around 100 °C and it is possibly related to some condensed moisture evaporation. The constant weight of the sample above 300 °C indicates that chemical reactions (e.g. oxidation) can be excluded in that range.

3.3. Procedures

All shear tests were performed at the same set of values of the major principal stress, σ_1, in the range 1000–1700 Pa by following almost the same procedure described by Chirone et al. [28] and here summarized. After filling, the bottom ring of the cell was mounted on the shear tester bench with the lid. The three thermocouples were inserted in the dedicated openings. The cell was loaded with the weights to be used in the consolidation step. The cell was kept still, while the heaters were turned on and the desired operating temperature was reached. The subsequent sequence of operations, carried out at the set temperature, mainly followed the standard procedure used to evaluate the yield locus in a standard Schulze Ring Shear Tester [58]. The same sample of powder was used to evaluate four different yield loci. Each yield locus was measured at least four different times on differently prepared samples. These allowed deriving four points of the flow function at the set temperature. Because of the limited availability of the material, only 500 g for each sample, a different use of the samples was required with respect to the procedure followed by Chirone et al. [28] who used a fresh sample every time the cell was filled again. In fact, each flow function test required about 100 g of material (without repetitions) and therefore it was necessary a sample "regeneration procedure", in order to use the same powder in more than a single test. According to this procedure, the sample was removed from the cell and brought inside a glove-bag in a nitrogen atmosphere. The purpose was to minimize the time exposure of the powder to oxygen. In the glove bag, all the clumps were broken up (or sieved out) by using two sieves (200 and 90 μm) through which the powder was let flow. The material obtained was re-used for other shear experiments at the same temperature or higher than the previous experiment. This procedure tended to minimize the effects of the sample cooling in the compacted state that had been reached within the cell in the previous experiment, and to bring it back to a condition that should be more similar to the loosely compacted state at which these powders were generated. In any case, memory effects should be limited for the reuse of powder from tests at temperatures in which there was no evidence of capillary bridging.

With each material a first set of experiments was performed by repeating at spaced temperature increments (25 → 150 → 300 → 340 → 380 → 420 → 460 → 500 °C) a binary sequence of a single pre-shear step at 600 Pa of normal load and a single shear step at 500 Pa of normal load. This test is useful in order to provide information on the temperature at which the rheological properties would change. The increments are set closer, at 40 °C differences, above 300 °C in the range of temperatures where the industrial application of the tested material provided indication of significant temperature effects.

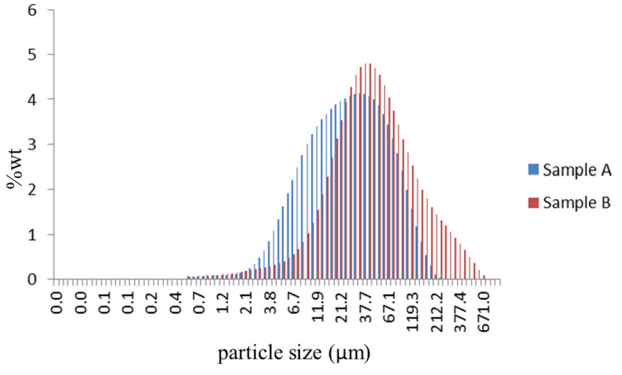

Fig. 3. PSD samples A and B.

4. Results and discussion

4.1. Experimental results

The results of the tests provided by a single pre-shear and a single shear of the yield loci at the same consolidation level and the same normal load during shearing increasing the temperatures (25 → 150 → 300 → 340 → 380 → 420 → 460 → 500 °C) are reported in Figs. 7 and 8. Inspection of Fig. 7 shows that the values obtained for the pre-shear stress and the shear stress at the same temperature differ below 400 °C. At temperatures between 400 °C and 500 °C these values are practically overlapped. This is an indication of the fact that the nature of the interparticle interactions is changing with the temperature. It is hypothesized that this change is due to the onset of capillary bridges between particles. In fact, the reduced effect of consolidation on the shear is in agreement with previous research [25] on the presence of capillary forces. A phenomenological interpretation of this finding can be guided by Eq. (1). This can be strictly applied to relate the material tensile strength with the average set of interparticle forces. It is clear from Eq. (1) that the strength of the material with consolidation can increase either because of the increase of the average forces F_{int} holding together two neighbouring particles, or because of the increase of the number of contact points per unit volume $\propto(1-\varepsilon)/\varepsilon$, consequent to powder densification. Considering van der Waals forces in which $F_{int} = F_{vdW}$, it is clear from Eq. 2 that consolidation can activate both the increase of the number of contact points and the increase of the

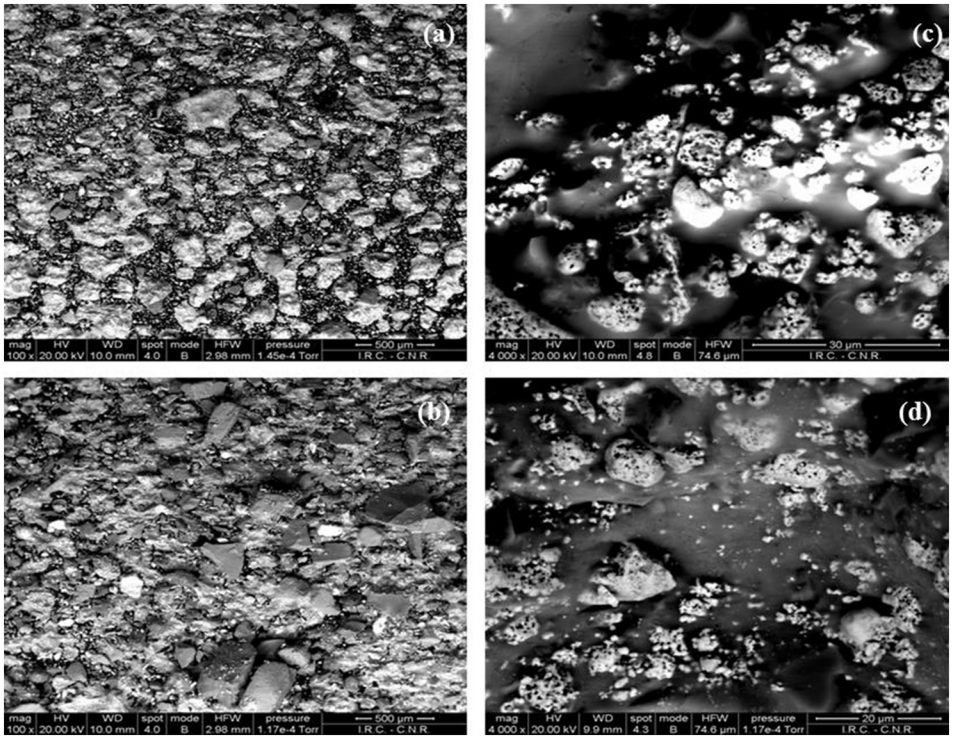

Fig. 4. SEM pictures for the sample "A" (a, b), "B" (c, d).

contact force, due to the significance of the effect of the plastic deformation of the contacts points due to the consolidation force F_N on the resulting value of F_{vdW}. Instead, for capillary forces $F_{int} = F^*_c$, inspection of the set of Eqs. (3) to (6) and the physics of the capillary bridge suggest that the binary interparticle forces are not directly affected by the normal consolidation forces F_N. Therefore, for capillary forces, the powder consolidation can change only as a result of a change in the powder porosity. As above mentioned, Eq. (1) is not valid for shearing. However, it is reasonable to hypothesize that the qualitative dependencies found above between consolidation and material strength can apply to the shear experiments reported in Figs. 7 and 8. Assuming that in these experiments the system porosity is not changing significantly during the test, the observed changes of shear stress are likely to mostly depend on changes in the interparticle forces. In particular, the increase of shear stress at certain temperature, as well as the reduced dependency of shear stress with the preshear consolidation, are both coherent with the onset of capillary forces, stronger than van der Waals forces and less affected by consolidation.

Taking the indication provided from these experiments, material yield loci and flow functions were measured at 25, 350, 450 and 500 °C in order to better describe the effect of temperature.

An example of the observed effect of temperature on the yield loci is reported in Fig. 9. For the sake of brevity Fig. 9 reports only results for a single material (sample B), two consolidation levels and two temperatures. The yield loci estimate in Fig. 9 were obtained combining the shear data coming from all the 4 independent repetitions of the test. All the other measured yield loci are available as additional material to this report. Also other data are available from the shear stress experiment, such as the powder porosity in each preshear and shear conditions. Also, these are not reported for the sake of brevity. In order to

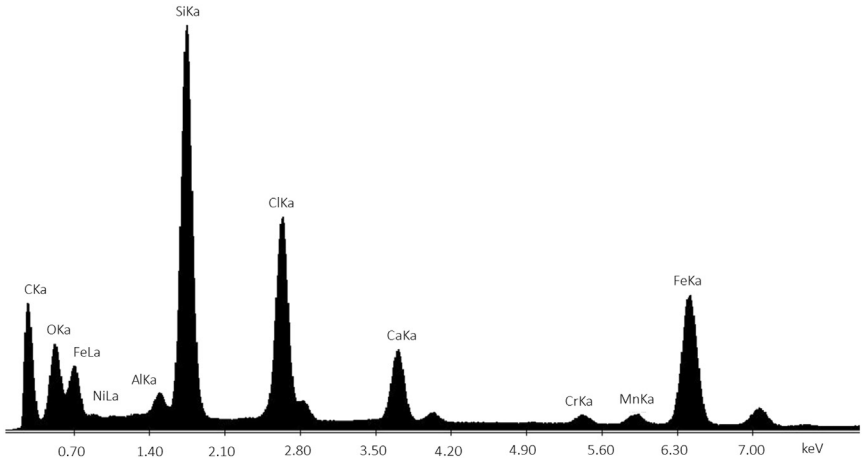

Fig. 5. EDX results for the sample "A".

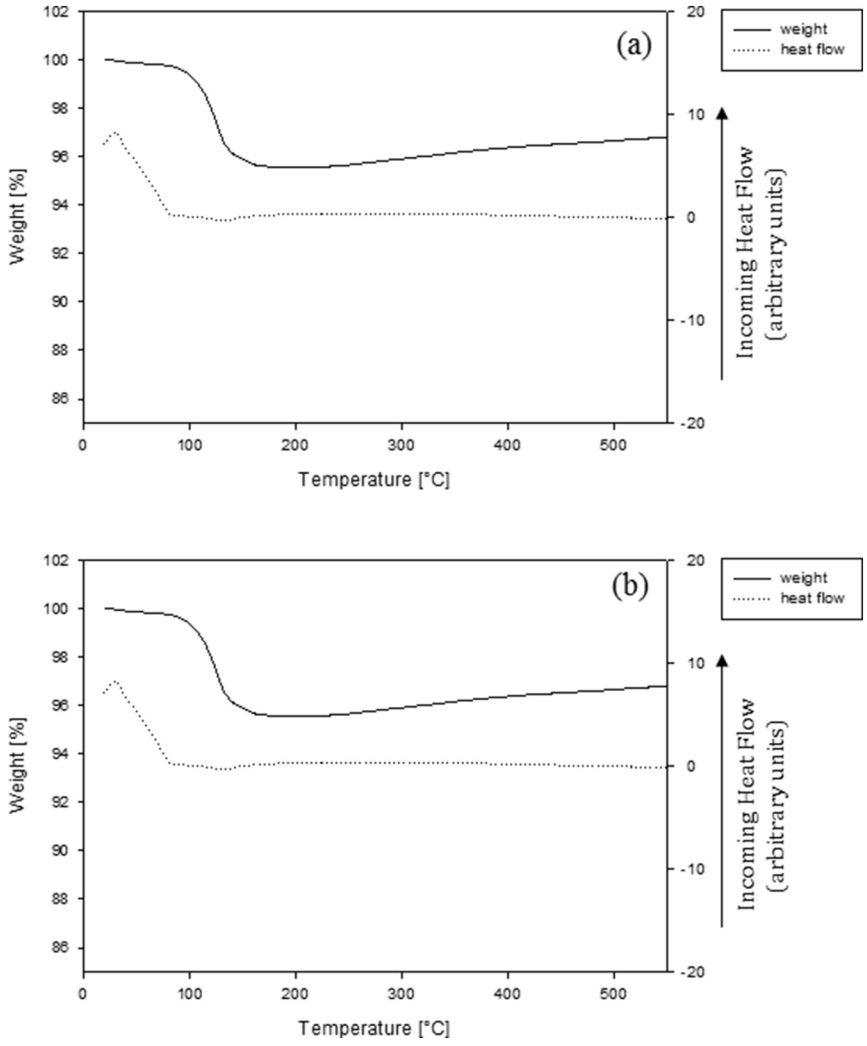

Fig. 6. Heat flow from DTA and sample weight from TGA plotted as a function of temperature: (a) Sample "A"; (b) Sample "B".

visualize the yield loci, the simple line description of the yield locus of Coulomb materials has been used:

$$\tau = C + \sigma \tan\varphi \tag{7}$$

where C, the yield locus intercept, is the material cohesion and φ, providing the slope of the yield locus tan φ, is the static angle of internal friction. The use of Eq. (7) allows to analyse the effect of temperature on τ by looking separately at the effect of temperature on C and φ.

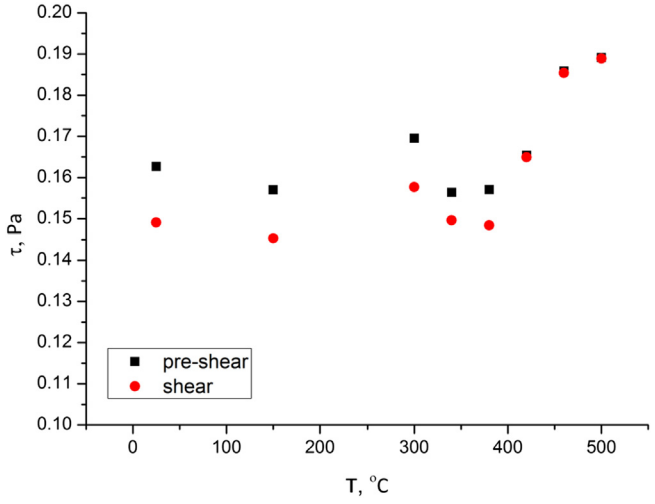

Fig. 7. Tests provided at each temperature by a single pre-shear step at 600 Pa of normal load and a single shear step at 500 Pa of normal load for Sample "A".

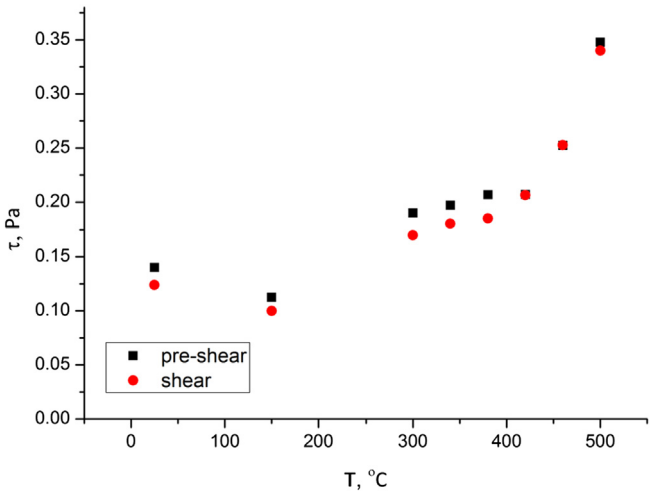

Fig. 8. Tests provided at each temperature by a single pre-shear step at 600 Pa of normal load and a single shear step at 500 Pa of normal load for Sample "B".

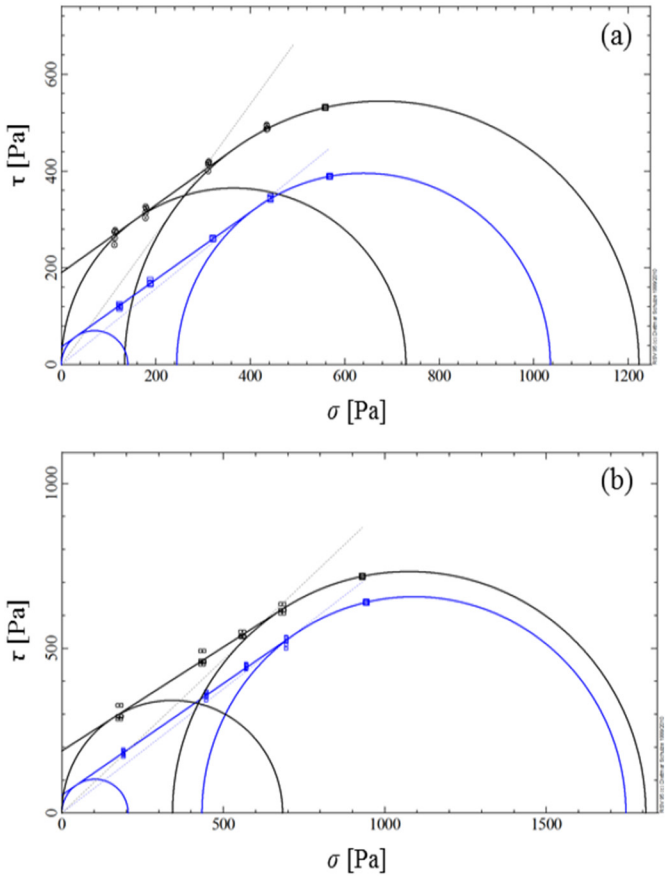

Fig. 9. Yield loci for the "B" sample measured with HT-ASC at 25 °C (blue line) and 500 °C (black line): (a) $\sigma_1 \approx 1000$ Pa; (b) $\sigma_1 \approx 1700$ Pa.

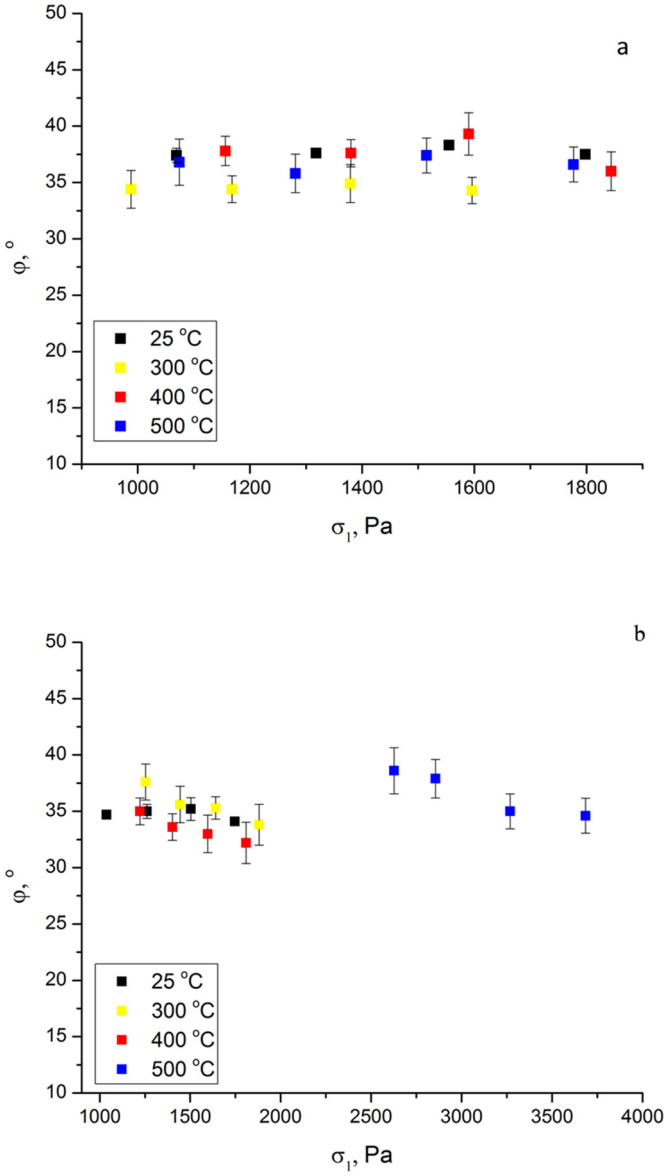

Fig. 10. Static angle of internal friction as a funtion of the consolidation stress and of the test temperature for: (a) sample "A" and (b) sample "B".

Beside the data points and the continuous straight lines representing the yield loci, Fig. 9 reports the Mohr circles representing the state of stress during consolidation (the larger circle on the right of the yield locus) and the Mohr circle representing the state of stress in an unconfined yield (the smaller circle on the right). The intercept of the consolidation Mohr circle with the σ axis, providing the larger value of σ is the point representing the stress on the major principal stress, σ_1, and acting in the corresponding principal direction. The value of σ_1 is commonly used to identify the consolidation condition. In the Figure, dotted lines passing through the origin and tangent to the consolidation Mohr circle define with their slope the effective angle of internal friction, used in many design procedures. More diffused details on yield loci and their derived powder flow properties are available elsewhere [62,63]. Inspection of Fig. 9 reveals that the cohesion C is significantly affected by both consolidation and temperature. On the contrary, the static angle of internal friction φ turns out to be almost independent of both consolidation and temperature. This is a behaviour typically shown by yield loci of powders showing prevailing capillary forces with amounts of liquid corresponding to the pendular state [25,26]. In these conditions, capillary forces are able to affect cohesion due to the increase of the adhesion forces between particles, but are not able to affect significantly the powder friction. Therefore, the observed increase of the unconfined yield strength, f_c, with both consolidation and temperature is to be attributed the cohesion changes for both the samples tested.

Fig. 10 summarizes all the values of the internal friction derived from the material yield loci obtained for both the materials at all the consolidation levels and temperatures at which the yield loci were determined. Error bars are also provided in Fig. 10. These were calculated as the maximum deviation of the values of the internal friction calculated separately for each of the 4 test repetitions. The same approach to calculate the error bars was used with the other flow parameters reported in Figs. 11 to 13 in the following. According to Fig. 10, the value of the angle of internal friction is about $35^{\circ} \pm 3^{\circ}$ and it does not change significantly with temperature.

Similar results are reported in Fig. 11 for the cohesion C. With reference to the sample A with a lower amount of impurities, the increase of temperature up to 300 °C does not produce any significant effect. At these temperatures, the cohesion is rather stable around 52 ± 7 Pa. At 400 °C, the cohesion rises to 87 ± 10 Pa and at 500 °C it rises up to 205 ± 15 Pa. The other powder sample, the one with higher amounts of impurities also exhibits a qualitatively similar behaviour. According with Fig. 11b, the cohesion for sample B at ambient temperature is around 42 ± 5 Pa. It is 142 ± 70 Pa at 300 °C and 183 ± 7 Pa at 400 °C. Tests performed at 300 °C exhibit a large scatter between data. This scatter is coherent with the interpretation of incipient formation of liquid capillary bridges that, close to the material melting condition, may make the measurement strongly variable between tests. In fact, shear

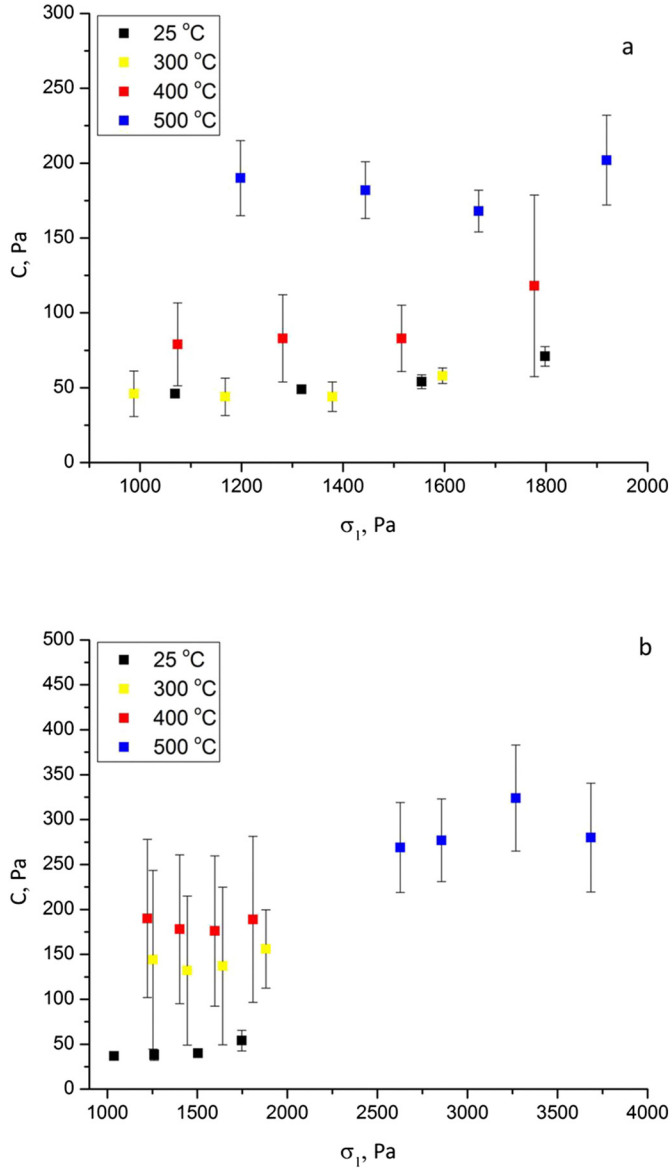

Fig. 11. Powder cohesion as a funtion of the consolidation stress and of the test temperature for: (a) sample "A" and (b) sample "B".

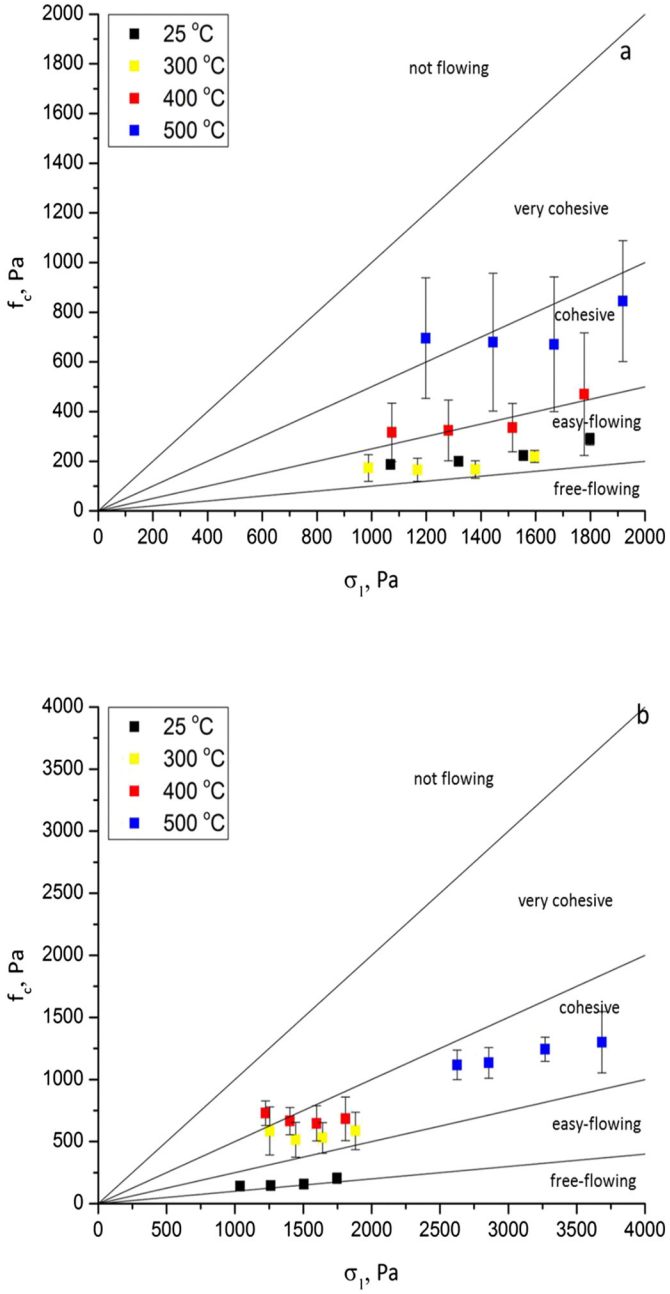

Fig. 13. Flow functions measured at different temperatures: (a) sample "A"; (b) sample "B".

stress results might be differently affected by the effective amount of the liquid phase formed. At 500 °C, it was not possible to perform the shear test at very low σ_1 (around 1000 Pa) because of a significant increase of

Fig. 12. Images of the cell during a test at a value of 1900 Pa of applied normal stress. On the left the lid lifted during the test. On the right the caked material in the lid vanes after the cell cooling.

the interparticle forces acting in the system. The presence of these forces at low values of normal load may result in a tensile force, which causes an irregular upward motion of the lid of the shear cell, as shown in Fig. 12. Therefore, the tests were performed at larger value of σ_1 (2600–3600 Pa). In these conditions, the results show a very high cohesion equal to 288 ± 17 Pa.

Table 3 reports the flow properties (namely, the cohesion C, the angle of internal friction φ, the unconfined yield strength f_c and the flow factor ffc) obtained as a function of temperature for both samples. Data in the table are limited to the lowest and the highest consolidation level. Instead, Fig. 13 reports the complete flow functions at different temperatures. According with Jenike [64], consolidated powders can be classified with respect to their flow behaviour using the flow factor, $ffc = \sigma_1/f_c$. In particular, Jenike [64] introduced 5 different regions of flowability, those of hardened materials ($ffc < 1$), very cohesive powders ($1 < ffc < 2$), cohesive powders ($2 < ffc < 4$), easy flowing powders ($4 < ffc < 4$) and free flowing powders ($ffc > 10$). These regions and the corresponding separation lines are reported in Fig. 13. In case of sample "A", inspection of Table 3 and of Fig. 13a indicates that the yield loci at ambient and 300 °C are almost coincident. This suggests that temperature changes have a minor effect on the powder cohesion in this range. Given the powder flow functions, for temperatures up to 300 °C, the powder can be classified as easy flowing. A significant increase of cohesion, around two times, is registered with increasing temperature up to 400 °C, nonetheless, the angle of internal friction does not show any significant change (about 35°). As a result, the upward shift of the flow function determines a classification change of the powder flow from easy flowing to cohesive. A further increase of temperature up to 500 °C produces an even larger cohesion and, therefore, a further upward shift of the flow function. For the sample "B", an increase of temperature from ambient to 300 °C involves an increase of cohesion of about four times its ambient value, resulting in an upward shift of the flow function from the easy flowing class to the limiting region between very cohesive and cohesive classes, as reported in Fig. 13b. For this powder, the yield loci at 300 °C and 400 °C are almost coincident. At 500 °C a strong powder bulk agglomeration was observed.

4.2. Model results

The particles used in this study have an irregular shape and, therefore, the effective curvature radius at the contact point that enters in the estimates of both van der Waals and capillary forces is not necessarily related to the particle size as, instead, it would happen for spherical particles. In order to overcome this system indeterminacy, the effective curvature radius at the contact was determined at ambient temperature using the approach previously followed by Chirone et al. [28], by making the hypothesis that in these conditions the capillary forces can be neglected. The curvature radius obtained with this procedure was then used to calculate the forces at other temperatures. The details of the procedure are reported below.

The isostatic tensile strength of the material was estimated from Coulomb Yield locus:

$$\sigma_t = \frac{C}{\tan\varphi} \tag{8}$$

The values of σ_t obtained from Eq. (8) are reported in Table 3. With the experiments, these values are used to evaluate the interparticle forces F_{int} from Eq. (1), considering the experimental values of the bed porosity ε in the shear experiment and the powder mean Sauter diameter d_{sv}. According to Molerus [9], the consolidation force at the contact point is estimated from the major principal stress during consolidation σ_1, reversing Eq. (1), and using the porosity of the preshear experiment:

$$F_N = \frac{d_{sv}^2\,\sigma_1\varepsilon}{1-\varepsilon} \tag{9}$$

Fig. 14 reports the values of F_{int} as a function of Aluminum Chloride is a low melting salt that alone sublimates at 180 °C and mixed with Ca F_N calculated according to the above procedure for both materials and at the different temperatures. As it appears, at high temperature interparticle forces increase of an order of magnitude with respect to ambient conditions (Fig. 14).

Considering only results at ambient temperature, Eq. (2) is used in order to calculate the average particle curvature radii at the contact point from the previously calculated value of $F_{int} = F_{vdW}$. The values of the material parameters used in Eq. (2) are listed in Table 4. The curvature radii obtained at ambient temperature for powder A and powder B are $8.85{\cdot}10^{-2}$ μm and $1.29{\cdot}10^{-1}$ μm, respectively. Chirone et al. [28] applied this procedure to estimate the effective curvature radii on sieved samples of a powder of fresh material, the same material of powder A and B, taken before the industrial use and not bearing surface impurities. In that case, the obtained value of the curvature radius at ambient temperature allowed predicting the different effects of consolidation and temperature on the experimental values of σ_t calculated with Eq. 8, by using Eqs. (9), (2) and (1) in sequence with the proper value of p_f estimated at the different temperatures. In the present study, the

Table 3
Results of the shear tests performed at different temperatures.

Sample sieving range	T [°C]	σ_1 [Pa]	C [Pa]	φ [deg]	f_c [Pa]	σ_t[Pa]	ffc [−]
Sample A	20	1069	46	37	187	60	5.76
	300	988	46	35	173	67	5.70
	400	1074	79	36	316	105	3.40
	500	1156	139	37	568	179	2.03
	20	1798	71	37	289	92	6.22
	300	1596	58	35	219	85	7.28
	400	1777	118	37	470	158	3.78
	500	1844	180	36	706	247	2.61
Sample B	20	1037	37	35	142	53	7.28
	300	1254	144	37	585	187	2.73
	400	223	190	35	729	271	1.68
	500	2626	269	38	1118	344	2.05
	20	1747	54	34	205	79	8.52
	300	1881	156	34	586	233	3.21
	400	1808	189	33	684	300	2.65
	500	3684	280	35	1067	407	3.45

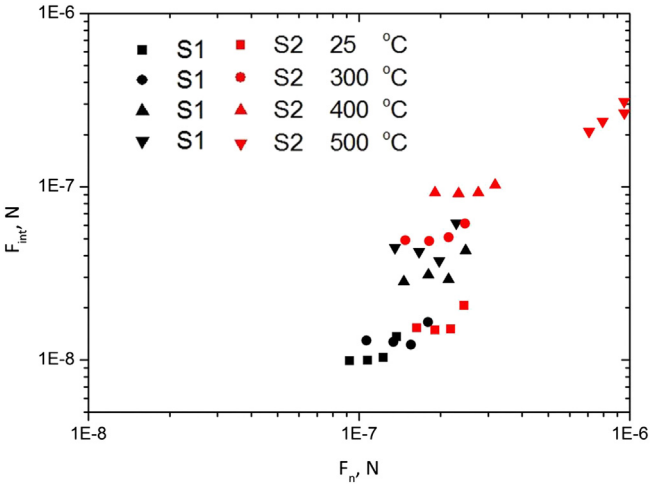

Fig. 14. Values of interparticle forces F_{int} calculated from experimental data according to Eqs. (1) and (8) as a function of the Normal Force F_N calculated according to Eq. (9) for the two materials and the different temperatures.

Table 4
Material parameters used in the model calculations.

Sieving range, μm	T °C	A^* 10^{-20} J	p_f GPa	ρ_p kg/m^3
Sample "A"	25	20	12	2330
	500	20	45	2320
Sample "B"	25	20	12	2330
	500	20	45	2320

same approach has been followed, but the model was not able to produce satisfactory predictions as it is shown in Fig. 15.

This result suggests that in the present study van der Waals forces alone are not able to explain the great increase of the cohesiveness of the particles with temperature. Therefore, a different procedure was followed to describe the effect of temperature, which made use of capillary interparticle forces. The fundamental hypothesis behind this approach is that the liquid phase on the surface is generated by the partial melting of the salt impurities present on the particle surfaces itself and described above with the materials (Section 3.2). In fact, the salts making the impurities, depending also on the composition of the mixture, can melt at temperatures that are much lower than the particle melting temperature that, in turn, is much higher than the tested temperatures. Therefore, it can be excluded that any liquid phase might contain the mother particle material. Necessary information to predict the capillary forces is the average volume of the liquid bridge V_b. Once V_b is known, the set of Eqs. (3) to (5) can be solved for r_1, r_2 and β, which in turn can be used to calculate the capillary force with Eq. (6).

The volume of the bridge was estimated using the quantitative analysis on the salt content of these powders. The weight fraction of the total salts in the samples, as well as the salt composition is reported in Table 5. The impurities have been characterized using the X-ray Fluorescence (XRF) and X-ray Diffraction (XRD) analyses. The results are reported in Table 5, in the columns in which the salt concentration base is "100 g of oxidized powder" columns. Due to the high tendency of Aluminum Chloride to be oxidized during the sample preparation procedure for the analytical determination, it is assumed that all the aluminum present in the quantitative analysis as alumina is present as Aluminum Chloride ($AlCl_3$). This assumption allows calculating the mass and the mole contents of the most abundant salts in 100 g of powder as reported in columns called "100 g of reduced powder" of Table 5.

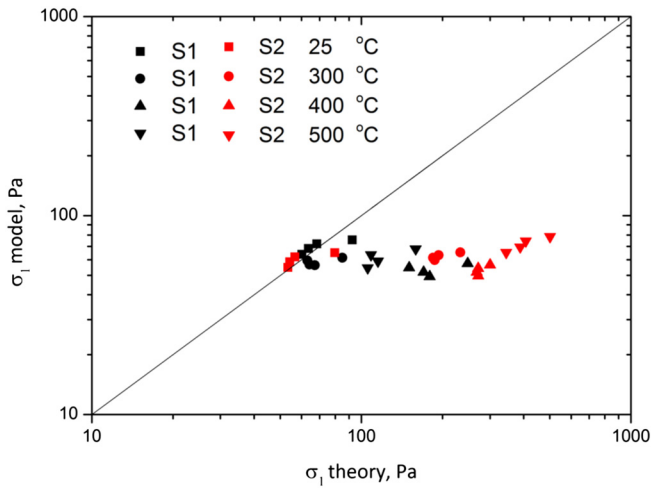

Fig. 15. Extrapolated tensile strength vs experimental tensile strength with the hypothesis of only van der Waals forces active.

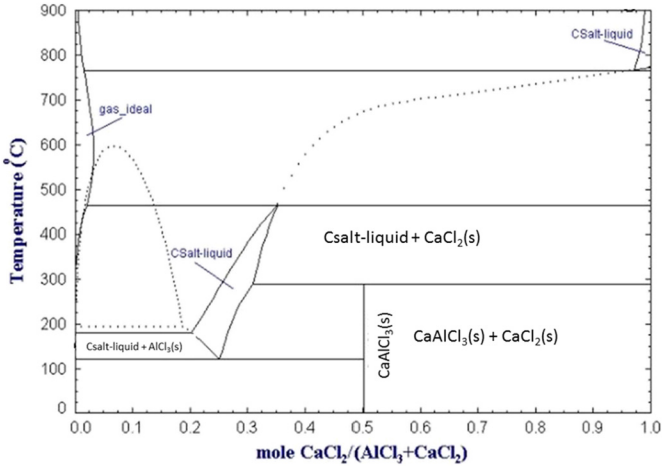

Fig. 16. Phase diagram of the salt binary sytem $AlCl_3$ + $CaCl_2$ [65].

Aluminum Chloride is a low melting salt that alone sublimates at 180 °C and mixed with $CaCl_2$, is able to melt at temperatures between 120 and 460 °C as shown in the phase diagram of the mixtures of the two salts, Fig. 16 [65]. In order to use the diagram, the mole fractions of the salt binary system $AlCl_3$ + $CaCl_2$ have been evaluated and they are reported, for the two samples, in the columns named "$AlCl_3$ + $CaCl_2$ in reduced powder" of Table 5.

With these compositions it is possible to use the phase diagram of Fig. 16 [65] and it is possible to calculate the liquid weight fraction (X_l) of the $AlCl_3$ + $CaCl_2$ systems, reported in Table 4. Provided the total salt weight fraction S_{tot} calculated for the system ($AlCl_3$ + $CaCl_2$) and given in the columns '$AlCl_3$ + $CaCl_2$ in reduced powder' of the last line of Table 5 it is possible to calculate the liquid volume per unit mass of the sample, V_l.

$$V_l = \frac{X_l \; S_{tot}}{\rho_{l\,a}} \tag{9}$$

Consequently, the amount of liquid per particle, L_p:

$$L_p = V_l V_p \rho_p \tag{10}$$

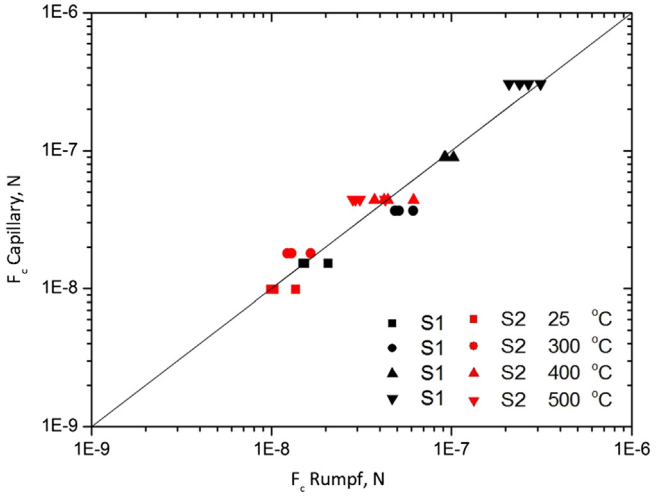

Fig. 17. Tensile strength of the liquid bridge calculated from the theory of capillary bridges vs the tensile strength of the liquid bridge estimated from the flow properties using Eq. (1).

Table 5
Salt composition in the powder samples.

Base	Sample "A"				Sample "B"			
	100 g of oxidized powder	100 g of reduced powder		$AlCl_3 + CaCl_2$ in reduced powder	100 g of oxidized powder	100 g of reduced powder		$AlCl_3 + CaCl_2$ in reduced powder
Mass	g	g	mol	mole fraction	g	g	mol	Mole fraction
Al_2O_3	1.8		–	–	3.1		–	–
$AlCl_3$	–	4.71	0.0353	0.247	–	8.11	0.0608	0.327
$FeCl_2$	2.3	0.35	0.0027	–	5.2	0.98	0.0077	–
$CaCl_2$	78.7	11.96	0.1078	0.753	73.4	13.87	0.1250	0.673
Salt/powder, wt%	15.2	17.0	17.0	16.7	18.9	22.3	22.3	22.0

and the average liquid volume per unit surface, λ_l, calculated using the mean Sauter diameter, d_{sv}, is

$$\lambda_l = \frac{L_p}{A_p} = V_l \frac{d_{sv}}{6} \rho_p \tag{11}$$

Resulting values for V_l, L_p and λ_l are reported in Table 6. In order to estimate the amount of surface liquid that is available for each bridge, we assumed that the bridge is able to collect the liquid on the portion of the asperity surfaces on which the liquid layer is able to touch the surface of both contacting particles. According to Fig. 1b this assumption defines an area of radius r_{cb} such that:

$$r_{cb} = \sqrt{(r_{pla} + \lambda_l)^2 - (r_{pla})^2} \tag{12}$$

And, in turn, it allows estimating the volume of the liquid that can form the liquid bridge V_b

$$V_b = \lambda_l \pi r_{cb}^2 \tag{13}$$

According to Eqs. (12) and (13), V_b can be calculated from λ_l once a certain asperity radius is assumed. The asperity radius calculated by the application of Eqs. (1) and (2) and reported in Table 6 was used on this purpose and also to solve the set of Eqs. (3) to (5) to evaluate r_1, r_2 and β and to calculate the tensile force of the bridge F_c^* with Eq. (6). Values of F_c^* are reported in Table 6. The surface tension of the mixture has been evaluated as the weighted average over the density of the single liquid components. Table 6 reports the value of the surface tension and liquid density for the two samples at different temperatures [66–69].

The tensile strength values obtained by using Eq. (1) and assuming $F_{int} = F_c^*$ were compared with the values obtained with the experimental tensile strength values in the parity plot of Fig. 17. The comparison shows a very good match between model values and experimental values for the two samples over a significantly large range of temperature tested, in spite of the large number of and assumptions made. These results allow concluding that, by assuming that capillary bridges are formed between two particle asperities and a reasonable value of the surface tension of the mixture, the model is able to correctly predict the order of magnitude of the tensile strength and its variations with temperature.

5. Conclusions

A set of experiments on the flow properties of two ceramic materials taken from a high temperature fluidized bed reactor was carried out at different temperatures from ambient up to 500 °C. Similar results in terms of temperature effects on the powder flow properties were found for the two materials differing for the amount of the contained impurities. SEM Images have localized the impurities on the particle surfaces. Shear test experiments show changes of the flow properties at high temperatures. The powder cohesion is the parameter which appears to be mostly affected by temperature while the angle of internal friction shows a weaker dependence on temperature and consolidation level. At high temperatures, the shear stress becomes almost independent of the consolidation state. These findings together with the nature of the impurities characterized by means of EDX analysis applied to SEM imaging strongly suggest that the observed changes are due to the occurrence of capillary bridges between particles, even if DTA and TGA are not able to detect any significant phase changes. However, the small amounts of liquid phase formed and confined to the particle surface are sufficient to considerably change the powder flow properties. The chemical analysis of the impurities allowed to identify the couple of most abundant salts that can produce a molten phase in the ranges of temperatures tested. The liquid phase produced and the estimation of the amount of liquids present in the capillary bridges based on geometrical consideration, together with a reasonable estimate of the liquid surface tension allows to correctly predicting the capillary interparticle forces and the tensile strength of the material.

These results also suggest the potential use of the HT-ASC as a sensitive detection instrument for phase changes limited to the particle surface also in particulate systems and conditions used in fluidized bed reactors. More in general the results indicate that shear testing results at ambient and high temperatures allow to correctly estimate the intensity of interparticle forces in particulate systems.

Table 6
Results of the model calculation.

Sample	T °C	r_{pla} 10^{-2} μm	X_{lCaCl2} -	X_l -	ρ_{la} kg m^{-3}	σ_s N/m	V_l 10^{-5} m^3 kg^{-1}	λ_l, μm	V_b 10^{-2} μm^3	Fc^* nN
A	25	8.85	–	–	–	0.140	–	–		9.89
	300		0.27	0.39	1330	0.050	5.06	0.25	8.49	18.0
	400		0.29	0.40	1080	0.175	5.17	0.26	9.57	43.9
	500		0.31	0.41	700	0.160	5.26	0.27	10.5	442
B	25	12.9	–	–	–	0.140	–	–		15.2
	300		0.27	0.51	1330	0.040	6.68	0.55	76.0	36.8
	400		0.29	0.53	1080	0.162	6.82	0.56	80.4	89.5
	500		0.31	0.54	700	0.160	6.94	0.57	84.2	306

Acknowledgements

Authors are grateful for the financial support provided by our industrial partner and wish to thank Mr. Luciano Cortese of the IRC-CNR in Naples for his contribution in providing high quality SEM analyses.

Nomenclature

a	gap between the asperity; μm
A	parameter in Eq. (2); N
A^*	Hamaker constant; N m
A_{bridge}	surface of the bridge; m^2
C	powder cohesion; Pa
d	particle diameter; μm
d_{10}	10th percentile particle size; μm
d_{32}	surface weighted mean particle size; μm
d_{43}	volume weighted mean particle size; μm
d_{50}	50th percentile particle size; μm
d_{90}	90th percentile particle size; μm
d_{sv}	particle Sauter mean diameter; μm
F_c	mean isotropic contact force; N
f_c	unconfined yield strength; Pa
F_c^*	tensile force of the bridge; N
ffc	flow factor
F_N	mean isotropic consolidation force at the particle contact; N
F_{vdW}	mean isotropic van der Waals force at the particle contact; N
K	coordination number
L_p	liquid per particle; m^3
N_p	number of particles
p_f	material compressive strength at particle contact; Pa
R	mean curvature radius at contact points; μm
r_1	external radius of the bridge; m
r_2	internal radius of the bridge; m
r_{cb}	radius of capillary bridge; m
r_{pla}	radius of the asperity; m
T	temperature; °C
V_b	volume of the bridge; m^3
V_l	volume of the liquid; m^3
$V_{l\ active}$	active volume for capillary bridge; m^3
X_l	liquid weight fraction in the salt system
z_0	interparticle separation distance; μm

Greek symbols

β	angle of the spherical cap of the contact; deg
γ_l	average liquid thickness; m
ε	porosity of the powder
ρ_b	bulk density; kg m^{-3}
ρ_{mix}	density of the mixture; kg/m^3
ρ_p	particle density; kg m^{-3}
σ	normal stress; Pa
σ_1	major principal stress; Pa
σ_c	normal stress at consolidation; Pa
σ_f	compressive yield strength; Pa
σ_s	surface tension; N/m
σ_t	tensile strength of the powder; Pa
τ	shear stress; Pa
φ	angle of internal friction; deg

Appendix A

The continuum approach is often used to describe powder mechanics in order to avoid the excessive complication and often the impossibility to describe the system by following the statics or the dynamics of the many single particles. For many technological applications it is useful, however, to understand and relate the properties of the material approached as a continuum with averaged particle-particle interactions. The main underlying assumptions behind the Rumpf [31] equation are:

1. Particles are organized in a randomly packed assembly.
2. Particles are spherical.
3. Particles are monodisperse.
4. The contact areas between particles are small enough in comparison with the particle surface and therefore contact areas can be assumed as contact points.
5. The contact points are distributed over the particle spherical surface with equal probability.
6. The packing structure is isotropic.
7. An isostatic state of stress, with three equal principal stresses, is assumed.
8. The coordination number (i.e., the mean number of contacts of a particle with the adjacent neighbours), k, and assembly porosity, ε, follow the correlation $k\varepsilon \approx 3.1 \approx \pi$ [58,70].

While it is easy to recognize that Assumptions 1, 4 and 5 can be easily verified for fine powders made of sufficiently stiff particles. All the other assumptions deserve some comment in order to be accepted with some confidence. In our case, the assumption that seems to be most strikingly in contrast with the real particles of the material used is the number 2, regarding the particle shape. In particular the spherical shape of the particles, together with the isostatic state of stress allow to assume that all forces acting on the particles are normal to the particle surface and directed towards or from the particle center. This condition is likely to be not verified in single cases of non-spherical particles. However, we have to recall that the Rumpf analysis approaches the stress description in terms of averaged interparticle forces. Therefore, it can be easy to recognize that, with random powder packings and isostatic states of stress, changes in the local force directions tend to compensate in the average, in the sense of leaving to a finite average value only the components directed towards the centre of mass of the particle. Similarly, since the particle size play the most important role in defining the number of interparticle contact points per unit volume, it can be easily acknowledged that violations of assumption 3 can be easily overcome by using the Sauter mean diameter as the average particle size. In fact, the Sauter averaging has the characteristic of keeping the same surface to volume ratio of the distribution and, therefore, also the same number of contact point per unit volume, that coincides also with the average number of interparticle forces contributing to the stress, the resulting force per unit area.

Of course the particle shape can affect also the how the number of contact points change with the porosity. However, it has to be recalled that the number of contact point per particle k, estimated by means of the relation $k\varepsilon = \pi$ [58,70], suggest numbers around 6 and 7 for powder porosities between 0.4 and 0.5. With the random packing of rather isometric particles, that is without any prevailing dimension such as those used in our systems, it is hard to think that deviation of k from π/ε may overcome the value of 1. According to Eq. (1) this would imply <15% error in the force/stress estimates. A fairly reasonable precision within the range of approximation of our calculations.

The most complex assumption to discuss is the n. 7 that indirectly supports also assumptions 5 and 6. In fact, Molerus [9] suggested that, since any isostatic tensile stress can be considered the combination of three uniaxial state of stress, and since any state of stress can be represented by three uniaxial state of stresses, then Eq. (1) can be applied to any state of stress. We suspect a flaw in this reasoning due to the fact that the first condition is necessary but not sufficient and, therefore, cannot be used as an equivalence, as the unflawed reasoning would require. In spite of that, we believe that Eq. (1) is still able to provide reasonable values of average normal stresses even in slightly non-isostatic conditions. This is the case of powder preshear, for which Eq. (1) is used to relate the normal consolidation stress (a value close to the average stress represented by the centre of the

consolidation Mohr circle) and the normal force consolidating the interparticle contacts.

Therefore, the approach proposed by Rumpf [31], in spite of the many assumptions required to find the extraordinary simple result reported in Eq. (1), still represents a reasonable and rather robust relation between average interparticle forces and local material stresses or strength that can be used also in systems with particles significantly differing from the assumed properties for his derivation.

References

[1] D. Kunii, O. Levenspiel, Fluidization Engineering, Butterworth-Heinemann, 1991.
[2] R.A. Newby, Applications for Gasifiers and Combustors, Chem. Ind. YORK-MARCEL DEKKER, 2003 397–420.
[3] U. Arena, L. Zaccariello, M.L. Mastellone, Fluidized bed gasification of waste-derived fuels, Waste Manag. 30 (2010) 1212–1219.
[4] J. Shabanian, J. Chaouki, Effects of temperature, pressure, and interparticle forces on the hydrodynamics of a gas-solid fluidized bed, Chem. Eng. J. 313 (2017) 580–590.
[5] P. Lettieri, D. Macrì, Effect of process conditions on fluidization, Kona Powder Part. J. (2016) 1–24, https://doi.org/10.14356/kona.2016017.
[6] W.B. Eisen, B.L. Ferguson, R.M. German, R. Iacocca, P.W. Lee, D. Madan, K. Moyer, H. Sanderow, Y. Trudel, Powder metal technologies and applications, https://www.osti.gov/scitech/biblio/289959 1998, Accessed date: 16 May 2017.
[7] C. Liang, X. Xie, P. Xu, X. Chen, C. Zhao, X. Wu, Investigation of influence of coal properties on dense-phase pneumatic conveying at high pressure, Particuology 10 (2012) 310–316, https://doi.org/10.1016/j.partic.2012.01.003.
[8] X. Fu, D. Huck, L. Makein, B. Armstrong, U. Willen, T. Freeman, Effect of particle shape and size on flow properties of lactose powders, Particuology 10 (2012) 203–208, https://doi.org/10.1016/j.partic.2011.11.003.
[9] O. Molerus, Theory of yield of cohesive powders, Powder Technol. 12 (1975) 259–275, https://doi.org/10.1016/0032-5910(75)85025-X.
[10] N. Pilpel, J.R. Britten, Effects of temperature on the flow and tensile strengths of powders, Powder Technol. 22 (1979) 33–44, https://doi.org/10.1016/0032-5910(79)85005-6.
[11] J. Tomas, Assessment of mechanical properties of cohesive particulate solids. Part 1: particle contact constitutive model, Part. Sci. Technol. 19 (2001) 95–110, https://doi.org/10.1080/02726350152772056.
[12] J. Tomas, Assessment of mechanical properties of cohesive particulate solids. Part 2: powder flow criteria, Part. Sci. Technol. 19 (2001) 111–129, https://doi.org/10.1080/02726350152772065.
[13] M. Medhe, B. Pitchumani, J. Tomas, Flow characterization of fine powders using material characteristic parameters, Adv. Powder Technol. 16 (2005) 123–135.
[14] R. Jones, H.M. Pollock, J.A.S. Cleaver, C.S. Hodges, Adhesion forces between glass and silicon surfaces in air studied by AFM: effects of relative humidity, particle size, roughness, and surface treatment, Langmuir 18 (2002) 8045–8055, https://doi.org/10.1021/la0259196.
[15] R. Jones, H.M. Pollock, D. Geldart, A. Verlinden-Luts, Frictional forces between cohesive powder particles studied by AFM, Ultramicroscopy 100 (2004) 59–78, https://doi.org/10.1016/j.ultramic.2004.01.009.
[16] A. Castellanos, The relationship between attractive interparticle forces and bulk behaviour in dry and uncharged fine powders, Adv. Phys. 54 (2005) 263–376, https://doi.org/10.1080/17461390500402657.
[17] M.A.S. Quintanilla, J.M. Valverde, A. Castellanos, Adhesion force between fine particles with controlled surface properties, AICHE J. 52 (2006) 1715–1728, https://doi.org/10.1002/aic.10770.
[18] C. Kanaoka, M. Hata, H. Makino, Measurement of adhesive force of coal fly ash particles at high temperatures and different gas compositions, Powder Technol. 118 (2001) 107–112, https://doi.org/10.1016/S0032-5910(01)00300-X.
[19] I. Tomasetta, D. Barletta, M. Poletto, The effect of temperature on flow properties of fine powders, Chem. Eng. Trans. 24 (2011) 655–660.
[20] D. Macrì, D. Barletta, P. Lettieri, M. Poletto, Experimental and theoretical analysis of TiO_2 powders flow properties at ambient and high temperatures, Chem. Eng. Sci. 167 (2017) 172–190, https://doi.org/10.1016/j.ces.2017.03.057.
[21] Y.Y. Liu, H. Lu, D. Barletta, M. Poletto, X. Guo, X. Gong, Y. Jin, Bulk flow properties of fly ashes at ambient and high temperature, Particuology (2017)https://doi.org/10.1016/j.partic.2017.04.013 (In press).
[22] Y. Liu, H. Lu, M. Poletto, X. Guo, X. Gong, Bulk flow properties of pulverised coal systems and the relationship between inter-particle forces and particle contacts, Powder Technol. 322 (2017) 226–240.
[23] Y. Liu, H. Lu, M. Poletto, X. Guo, X. Gong, Y. Jin, Flow properties and inter-particle forces in fuel powders, Particuology 34 (2017)https://doi.org/10.1016/j.partic.2016.10.007.
[24] P. Pierrat, H.S. Caram, Tensile strength of wet granular materials, Powder Technol. 91 (1997) 83–93, https://doi.org/10.1016/S0032-5910(96)03179-8.
[25] P. Pierrat, D.K. Agrawal, H.S. Caram, Effect of moisture on the yield locus of granular materials: theory of shift, Powder Technol. 99 (1998) 220–227, https://doi.org/10.1016/S0032-5910(98)00111-9.
[26] G. Landi, D. Barletta, M. Poletto, Modelling and experiments on the effect of air humidity on the flow properties of glass powders, Powder Technol. 207 (2011) 437–443, https://doi.org/10.1016/j.powtec.2010.11.033.
[27] T. Gröger, U. Tüzün, D.M. Heyes, Modelling and measuring of cohesion in wet granular materials, Powder Technol. 133 (2003) 203–215, https://doi.org/10.1016/S0032-5910(03)00093-7.
[28] R. Chirone, D. Barletta, P. Lettieri, M. Poletto, Bulk flow properties of sieved samples of a ceramic powder at ambient and high temperature, Powder Technol. 288 (2016) 379–387, https://doi.org/10.1016/j.powtec.2015.11.040.
[29] C.Q. LaMarche, A.W. Miller, P. Liu, C.M. Hrenya, Linking micro-scale predictions of capillary forces to macro-scale fluidization experiments in humid environments, AICHE J. 62 (2016) 3585–3597, https://doi.org/10.1002/aic.15281.
[30] T.O. Althaus, E.J. Windhab, N. Scheuble, Effect of pendular liquid bridges on the flow behavior of wet powders, Powder Technol. 217 (2012) 599–606, https://doi.org/10.1016/j.powtec.2011.11.026.
[31] H.C.H. Rumpf, Zur Theorie der Zugfestigkeit von Agglomeraten bei Kraftübertragung an Kontaktpunkten, Chem. Ing. Technol. 42 (1970) 538–540, https://doi.org/10.1002/cite.330420806.
[32] H.O. Kono, E. Aksoy, Y. Itani, Measurement and application of the rheological parameters of aerated fine powders — a novel characterization approach to powder flow properties, Powder Technol. 81 (1994) 177–187, https://doi.org/10.1016/0032-5910(94)02876-1.
[33] G. Bruni, P. Lettieri, D. Newton, D. Barletta, An investigation of the effect of the interparticle forces on the fluidization behaviour of fine powders linked with rheological studies, Chem. Eng. Sci. 62 (2007) 387–396, https://doi.org/10.1016/j.ces.2006.08.059.
[34] D. Geldart, Types of gas fluidization, Powder Technol. 7 (1973) 285–292, https://doi.org/10.1016/0032-5910(73)80037-3.
[35] J.M. Valverde, A. Castellanos, Fluidization of nanoparticles: a simple equation for estimating the size of agglomerates, Chem. Eng. J. 140 (2008) 296–304, https://doi.org/10.1016/j.cej.2007.09.032.
[36] J. Shabanian, J. Chaouki, Fluidization characteristics of a bubbling gas – solid fluidized bed at high temperature in the presence of interparticle forces, Chem. Eng. J. 288 (2016) 344–358, https://doi.org/10.1016/j.cej.2015.12.016.
[37] Takafumi Mikami, Hidehiro Kamiya, Masayuki Horio, The mechanism of defluidization of iron particles in a fluidized bed, Powder Technol. 89 (1996) 231–238, https://doi.org/10.1016/S0032-5910(96)03187-7.
[38] J.P.K. Seville, H. Silomon-Pflug, P.C. Knight, Modelling of sintering in high temperature gas fluidisation, Powder Technol. 97 (1998) 160–169, https://doi.org/10.1016/S0032-5910(98)00008-4.
[39] S.M.P. Mutsers, K. Rietema, The effect of interparticle forces on the expansion of a homogeneous gas-fluidized bed, Powder Technol. 18 (1977) 239–248, https://doi.org/10.1016/0032-5910(77)80014-4.
[40] O. Molerus, Interpretation of Geldart's type A, B, C and D powders by taking into account interparticle cohesion forces, Powder Technol. 33 (1982) 81–87, https://doi.org/10.1016/0032-5910(82)85041-9.
[41] K. Rietema, H.W. Piepers, The effect of interparticle forces on the stability of gas-fluidized beds – I. Experimental evidence, Chem. Eng. Sci. 45 (1990) 1627–1639.
[42] Q.F. Hou, Z.Y. Zhou, A.B. Yu, Micromechanical modeling and analysis of different flow regimes in gas fluidization, Chem. Eng. Sci. 84 (2012) 449–468.
[43] L. Massimilla, G. Donsì, Cohesive forces between particles of fluid-bed catalysts, Powder Technol. 15 (1976) 253–260.
[44] J.P.K. Seville, C.D. Willett, P.C. Knight, Interparticle forces in fluidisation: a review, Powder Technol. 113 (2000) 261–268, https://doi.org/10.1016/S0032-5910(00)00309-0.
[45] J. Visser, Van der Waals and other cohesive forces affecting powder fluidization, Powder Technol. 58 (1989) 1–10, https://doi.org/10.1016/0032-5910(89)80001-4.
[46] G.A. Turner, M. Balasubramanian, Investigations of the contributions to the tensile strength of weak particulate masses, Powder 10 (1974) 121–127.
[47] M.C. Coelho, and N., 20 (1978) 201–205.
[48] J.W.G. Tyrrell, J.A.S. Cleaver, The effect of atmospheric humidity on interparticle forces, Proc. 1997 Jubil. Res. Event IChemE, Nottingham. (n.d.) 541–544.
[49] Robert Jones, Hubert M. Pollock, Jamie A.S. Cleaver, C.S. Hodges, Adhesion Forces Between Glass and Silicon Surfaces in Air Studied by AFM: Effects of Relative Humidity, Particle Size, Roughness, and Surface Treatment, 2002https://doi.org/10.1021/LA0259196.
[50] M. D'Amore, G. Donsì, L. Massimilla, The influence of bed moisture on fluidization characteristics of fine powders, Powder Technol. 23 (1979) 253–259, https://doi.org/10.1016/0032-5910(79)87015-1.
[51] H. Schubert, Capillary forces - modeling and application in particulate technology, Powder Technol. 37 (1984) 105–116, https://doi.org/10.1016/0032-5910(84)80010-8.
[52] K. Johanson, Y. Rabinovich, B. Moudgil, K. Breece, H. Taylor, Relationship between particle scale capillary forces and bulk unconfined yield strength, Powder Technol. 138 (2003) 13–17.
[53] J.P.K. Seville, R. Clift, The effect of thin liquid layers on fluidisation characteristics, Powder Technol. 37 (1984) 117–129, https://doi.org/10.1016/0032-5910(84)80011-X.
[54] M. Wormsbecker, T. Pugsley, The influence of moisture on the fluidization behaviour of porous pharmaceutical granule, Chem. Eng. Sci. 63 (2008) 4063–4069, https://doi.org/10.1016/j.ces.2008.05.023.
[55] C.-L. Lin, M.-Y. Wey, The effect of mineral compositions of waste and operating conditions on particle agglomeration/defluidization during incineration, Fuel 83 (2004) 2335–2343, https://doi.org/10.1016/j.fuel.2004.06.030.
[56] J.N. Israelachvili, I.I. Part, The forces between particles and surfaces, Intermol. Surf. Forces, Elsevier 2011, pp. 191–499, https://doi.org/10.1016/B978-0-12-375182-9.10025-9.
[57] W.O. Smith, P.D. Foote, P.F. Busang, Packing of homogeneous spheres, Phys. Rev. 34 (1929) 1271–1274, https://doi.org/10.1103/PhysRev.34.1271.
[58] ASTMD6773-02, Standard Shear Test Method for Bulk Solids Using the Schulze Ring Shear Tester, 2008.
[59] L. Fayed, Muhammed Otten, Handbook of Powder Science & Technology, 2013.

[60] Y.I. Rabinovich, J.J. Adler, M.S. Esayanur, A. Ata, R.K. Singh, B.M. Moudgil, Capillary forces between surfaces with nanoscale roughness, Adv. Colloid Interf. Sci. 96 (2002) 213–230, https://doi.org/10.1016/S0001-8686(01)00082-3.
[61] I. Tomasetta, D. Barletta, M. Poletto, The high temperature annular shear cell: a modified ring shear tester to measure the flow properties of powders at high temperature, Adv. Powder Technol. 24 (2013) 609–617, https://doi.org/10.1016/j.apt.2012.11.007.
[62] R.M. Nedderman, Statics and Kinematics of Granular Materials, Cambridge University Press, 1992.
[63] D. Schulze, Powders and Bulk Solids, Springer, Berlin Heidelberg, Berlin, Heidelberg, 2008https://doi.org/10.1007/978-3-540-73768-1.
]64] A.W. Jenike, Gravity flow of solids, Trans. Inst. Chem. Eng. 40 (1962) 264.
[65] CRCT - École Polytechnique de Montréal - Génie chimique/Chemical Eng., http://www.crct.polymtl.ca/fact/phase_diagram.php?file=AlCl3-CaCl2.jpg&dir=FTsalt, (n.d.).
[66] G.J. Janz, C.B. Allen, N.P. Bansal, R.M. Murphy, R.P.T. Tomkins, Physical Properties Data Compilations Relevant to Energy Storage. II. Molten Salts: Data on Single and Multi-component Salt Systems, 1979 445http://www.dtic.mil/docs/citations/ADD095217.
[67] G.J. Janz, R.P.T. Tomkins, C.B. Allen, J.R. Downey, G.L. Garner, U. Krebs, S.K. Singer, Molten salts: volume 4, part 2, chlorides and mixtures—electrical conductance, density, viscosity, and surface tension data, J. Phys. Chem. Ref. Data 4 (1975) 871–1178, https://doi.org/10.1063/1.555527.
[68] T.D. Sokolova, L.A. Nisel'son, Density, viscosity, and surface tension of aluminum and gallium trichlorides, Russ. J. Inorg. Chem. 10 (1965).
[69] G.J. Janz, F.W. Dampier, G.R. Lakshminarayanan, P.K. Lorenz, R.P.T. Tomkins, Molten Salts: Vol 1, Electrical Conductance, Density, and Viscosity Data, 1968.
[70] H. Krupp, Particle adhesion theory and experiment, Adv. Colloid Interf. Sci. 1 (1967) 111–239, https://doi.org/10.1016/0001-8686(67)80004-6.